PONTIFICIA UNIVERSIDAD CATÓLICA DEL PERÚ

Escuela de Posgrado

Spatially Weighted Fidelity and Regularization Terms for Attenuation Imaging

Tesis para obtener el grado académico de Maestro en Ingeniería Biomédica que presenta:

Mauricio Sebastian Merino Acuña

Asesor:

Ph.D. Roberto Lavarello Montero

Lima, 2025

Informe de Similitud

Yo, Roberto Janniel Lavarello Montero, docente de la Escuela de Posgrado de la Pontificia Universidad Católica del Perú, asesor de la tesis titulado
Spatially Weighted Fidelity and Regularization Terms for Attenuation Imaging, del autor Mauricio Sebastian Merino Acuña, dejo constancia de lo siguiente:

- El mencionado documento tiene un índice de puntuación de similitud de 23%. Así lo consigna el reporte de similitud emitido por el software *Turnitin* el 15/08/2025.
- He revisado con detalle dicho reporte y la Tesis o Trabajo de Suficiencia Profesional, y no se advierte indicios de plagio.
- Las citas a otros autores y sus respectivas referencias cumplen con las pautas académicas.

Lugar y fecha:

Lima, 15 de agosto del 2025

Apellidos y nombres del asesor: Lavarello Montero, Roberto Janniel	
DNI: 10544227	Firma 
ORCID: https://orcid.org/0000-0001-8472-5161	

-
- Explicación del índice de similitud superior al 20%: el índice no excede el 1% para ninguna fuente salvo en el primer caso, que corresponde a un reporte del mismo alumno con un índice de 3%. En todos los casos, los textos resaltados se limitan a definiciones puntuales de conceptos generales relacionados al tema de estudio.

Resumen

La ecografía cuantitativa tiene potential para mejorar la precisión diagnóstica. La diferencia logarítmica espectral regularizada puede generar mapas de atenuación local precisos. Sin embargo, el rendimiento del método se degrada cuando se producen cambios significativos en la amplitud de retrodispersión. Se han introducido variaciones de la técnica que implican un enfoque ponderado de la regularización de la retrodispersión; sin embargo, no es eficaz cuando se producen cambios tanto en la atenuación como en la retrodispersión. Este estudio introduce un nuevo enfoque que incorpora una norma L1 para la regularización de la retrodispersión y ponderaciones que varían espacialmente para los términos de fidelidad y regularización. Los pesos se calculan a partir de una estimación inicial de los cambios de retrodispersión. Se realizaron análisis comparativos con datos simulados, de maniquíes y clínicos. Cuando se producen cambios en la retrodispersión y la atenuación, el enfoque propuesto redujo el error cuadrático medio más bajo hasta en un 73%. También mejoró la relación contraste-ruido en un factor de 4,4 de media en comparación con los métodos disponibles anteriormente, teniendo en cuenta los datos simulados y de maniquí. Los resultados *in vivo* obtenidos en hígados sanos, nódulos tiroideos y un tumor de mama confirman su eficacia. En el hígado, se muestra eficaz para reducir los artefactos de las imágenes de atenuación. En los tumores de tiroides y mama, el método demostró una mejor relación contraste-ruido y una mayor coherencia de las mediciones de atenuación con el realce acústico posterior. En general, este método es prometedor para mejorar las imágenes de atenuación por ultrasonidos, ya que ayuda a diferenciar las características de los tejidos que pueden indicar patología.

Palabras clave—ultrasonido cuantitativo, pendiente del coeficiente de atenuación, diferencia espectral logarítmica, imágenes de atenuación ultrasónica, regularización adaptiva.

Abstract

Quantitative ultrasound holds promise in enhancing diagnostic accuracy. For attenuation imaging, the regularized spectral log difference can generate accurate local attenuation maps. However, the performance of the method degrades when significant changes in backscatter amplitude occur. Variations of the technique were introduced involving a weighted approach to backscatter regularization; however, it is not effective when changes in both attenuation and backscatter occur. This study introduces a novel approach that incorporates an L1-norm for backscatter regularization and spatially varying weights for both fidelity and regularization terms. The weights are calculated from an initial estimation of backscatter changes. Comparative analyses with simulated, phantom, and clinical data were performed. When changes in backscatter and attenuation occur, the proposed approach reduced the lowest root mean square error by up to 73%. It also improved the contrast-to-noise ratio by a factor of 4.4 on average compared to previously available methods, considering the simulated and phantom data. *In vivo* results from healthy livers, thyroid nodules, and a breast tumor further confirm its effectiveness. In the liver, it is shown to be effective at reducing artifacts of attenuation images. In thyroid and breast tumors, the method demonstrated an enhanced contrast-to-noise ratio and better consistency of the attenuation measurements with the posterior acoustic enhancement. Overall, this approach offers promise for enhancing ultrasound attenuation imaging by helping differentiate tissue characteristics that may indicate pathology.

Keywords—quantitative ultrasound, attenuation coefficient slope, spectral log difference, ultrasound attenuation imaging, weighted regularization.

Dedicado a mis padres Delia y Arturo,
a mis hermanos Roger, Henry y Angie,
a mis amigos del Laboratorio de Imágenes Médicas
y a Mabel.

Acknowledgements

This thesis marks the culmination of my master's studies, and I would like to express my gratitude to my family and closest friends for their support throughout this journey. I extend my sincere appreciation to Professor Roberto Lavarello for welcoming me into the Laboratorio de Imágenes Medicas (LIM) and for his invaluable mentorship. I am also grateful to the LIM members and friends, especially Stefano Romero and Andres Coila, for their support.

Finally, I would like to acknowledge the funding that made this research possible. This thesis was funded by the Consejo Nacional de Ciencia, Tecnología e Innovación Tecnológica (CONCYTEC) through research grant N° PE501082070-2023-PROCIENCIA. This fund also enabled me to present my work at the 2024 IEEE Latin American Ultrasound Symposium in Montevideo, Uruguay (LAUS 2024); the 2024 IEEE International Symposium on Biomedical Imaging in Athens, Greece (ISBI 2024); and the 2025 IEEE International Symposium on Biomedical Imaging in Houston, Texas (ISBI 2025). I also extend my gratitude to Escuela de Posgrado PUCP for partially funding my travel expenses to ISBI 2024 and ISBI 2025, through an internal grant and Fondo Marco Polo, respectively.

Contents

List of Figures

List of Tables

Chapter 1

Introduction

1.1 Quantitative ultrasound

Quantitative characterization of biological tissues using ultrasound is increasingly relevant in clinical and research settings. Unlike conventional B-mode imaging, which provides qualitative, operator-dependent visual information, quantitative ultrasound techniques aim to extract physical tissue properties from the radiofrequency data [1]. Two of these properties are the acoustic attenuation and backscatter coefficients.

Attenuation coefficient

Ultrasound attenuation has been widely explored for tissue characterization and its potential diagnostic value. Generally speaking, attenuation refers to the loss of mechanical energy as an acoustic wave propagates in soft tissue. The effective attenuation along the propagation path from the source through the intervening tissues is known as total attenuation, and the term used to quantify the tissue properties at each region is local attenuation [2]. The frequency dependence of attenuation is modeled by a power law, which is commonly approximated as a linear relationship [3]. Its slope is known as the local attenuation coefficient slope (ACS).

There are various clinical applications of tissue characterization using the attenuation coefficient. The ACS has been extensively studied for staging liver steatosis [4], leading to its integration into certain ultrasound scanners for clinical use [5]. Other studies include attenuation measurements in thyroid [6], breast [7], uterine cervix [8], and placental tissues [9].

Backscatter coefficient

The backscatter coefficient (BSC) characterizes the time-averaged backscattered intensity per unit solid angle and unit volume, normalized by the time-averaged incident wave intensity [10]. It is inherently frequency-dependent, reflecting the intricate interaction of ultrasonic waves with the structural characteristics of the scattering medium. The BSC enables the evaluation of key parameters such as scatterer size [11] and acoustic concentration [12].

The applications of the backscatter coefficient span diverse areas in medical diagnostics and tissue characterization. The BSC has been extensively employed to differentiate

fatty versus healthy livers [13], and for characterizing thyroid tissue [14]. However, to estimate the backscatter coefficient, the total attenuation along the propagation path must be estimated [1].

1.2 Attenuation coefficient slope estimation

There are several techniques available for estimating ACS, which involve analyzing the frequency spectrum of the backscattered echoes [10]. These may be broadly classified into two categories: spectral shift [15, 16] and spectral difference [17] methods. The spectral shift methods analyze the downshift of the center frequency of the spectrum with depth, whereas spectral difference methods analyze the reduction in signal power with depth for all frequencies in the band of interest. Compensation of diffraction effects is typically accomplished using measurements from a calibrated phantom [18].

The spectral log difference (SLD) method analyzes the changes in the spectra in two continuous windows along the axial direction. Directly solving this inverse problem exhibits a significant trade-off between estimation accuracy and spatial resolution [19]. For this reason, Coila *et. al* proposed a regularization scheme based on total variation to generate denoised attenuation images [20]. However, it is well known that spectral methods for attenuation estimation exhibit a severely degraded performance at locations with moderate to large backscatter coefficient (BSC) discontinuities [21], resulting in significant artifacts that compromise the performance of regularized spectral methods.

Other approaches have also been developed for attenuation imaging. An algorithm was introduced to characterize attenuation as a power law [22], however, it exhibited higher variation compared to the spectral log difference technique [23]. Efforts to simultaneously characterize attenuation and backscatter have also been explored, using dynamic programming [24] and regularization [25, 26]. These approaches jointly estimate ACS and BSC using a power-law model for the latter. Nonetheless, these can exhibit higher variability due to the higher number of unknowns [27]. In addition, a reference-free approach for attenuation estimation was introduced, based on the assumption that diffraction effects vary negligibly between adjacent frequency components in imaging regions with slowly changing beam patterns, such as in plane wave imaging [28]. Subsequently, a regularized version of this method was proposed, incorporating adaptive frequency range selection and automatic regularization parameter tuning [29]. A drawback of these approaches is that they require a larger computing window, which compromises spatial resolution.

Weighted regularization approaches that produce spatially variant regularization coefficients have also been developed to improve results from spectral-based attenuation imaging techniques. In [30], weights are proposed to eliminate artifacts and variability in the ACS map generated by SLD. They are shown to be effective in heterogeneous media, but only when changes in either the backscatter or the attenuation coefficient occur. Similarly, a weighted regularized approach has also been employed to obtain a 1D estimate of ACS, which only maps axial variations [31]. However, it has not been generalized for attenuation imaging as it does not incorporate information from adjacent lateral windows and has only been tested in layered media. In addition, weighting the fidelity term has been shown to improve the estimation of the backscatter coefficient

using the reference phantom method [32]. The weights are based on the backscattered power spectra and vary by depth and frequency. Nonetheless, this has only been tested in media with uniform ACS. Media where both ACS and BSC vary simultaneously still represent a challenge in quantitative ultrasound.

1.3 Objectives

This study aims to present a new inverse formulation for SLD that can be applied to media that exhibit changes in both backscatter and attenuation. The specific objectives of this work are:

- To develop a robust inverse formulation that includes spatially varying weights for the fidelity and regularization.
- To implement and test the reconstruction technique with data obtained from simulations, experimental phantoms, and *in vivo* tissue data.
- To compare the performance of the implemented method with other state-of-the-art methods in terms of estimation error, variability, and contrast-to-noise ratio.

1.4 Overview of the document

Chapter 2, Theory describes the theoretical framework of the SLD technique and the regularization functions found in the literature, and describes the proposed approach.

Chapter 3, Methods describes the details regarding the datasets, implementation, and the metrics used to evaluate the performance of the proposed approach compared to other approaches.

Chapter 4, Testing and validation summarizes the results in each dataset and discusses them.

This thesis expands upon research originally presented at the 2024 IEEE International Symposium on Biomedical Imaging [33] and later published in IEEE Transactions on Ultrasonics, Ferroelectrics and Frequency Control [34].

Chapter 2

Theory

2.1 Spectral Log Difference (SLD)

The power spectrum of the echo signals $S(x, z, f)$, considering a window located at coordinates (x, z), can be modeled as

$$S(x, z, f) = P(f)D(x, z, f)\sigma(x, z, f)A_T(x, z, f), \tag{2.1}$$

where f is the frequency, $P(f)$ is the scanner transfer function, $D(x, z, f)$ represents the diffraction and beamforming effects, $\sigma(x, z, f)$ is the backscatter term, and $A_T(x, z, f)$ is the total ultrasound attenuation [20].

To cancel the parameters that depend on the transducer, the spectral log difference, centered at depth z, calculates the log ratio of two adjacent sub-blocks, located at depths $z+\Delta z/2$ and $z-\Delta z/2$. In this case, assuming that $A_T(x, z+\Delta z, f) = A_T(x, z, f)e^{-4\beta f \Delta z}$, where β is the ACS, the spectral log difference can be defined as

$$\begin{aligned} Y(x, z, f) &\triangleq \log\left[\frac{S(x, z+\frac{\Delta z}{2}, f)}{S(x, z-\frac{\Delta z}{2}, f)}\right] - D_r(x, z, f), \\ &= 4f\Delta z \cdot \beta(x, z, f) + c(x, z, f), \end{aligned} \tag{2.2}$$

where $D_r(x, z, f)$ accounts for diffraction effects and the term $c(x, z, f)$ is the log ratio of the backscatter term. This ratio is assumed to be independent of frequency. The diffraction can be estimated using the reference phantom method [18]. Given a reference with known frequency-dependent attenuation $\alpha_r(f)$, the diffraction ratio can be calculated with:

$$D_r(x, z, f) = \log\left[\frac{S_r(x, z+\frac{\Delta z}{2}, f)}{S_r(x, z-\frac{\Delta z}{2}, f)}\right] - 4\Delta z \cdot \alpha(f), \tag{2.3}$$

where S_r is the estimated power spectrum of the reference phantom.

2.2 Regularized Spectral Log Difference (RSLD)

Equation (2.2) is linear, so it can be written in a matrix form. Considering m, n and p as the number of points in the lateral, axial and frequency dimensions, the measurements

from the SLD can be vectorized in $\boldsymbol{y} \in \mathbb{R}^{mnp}$ and the unknowns (β and c) into a variable $\boldsymbol{x} \in \mathbb{R}^{2mn}$:

$$\boldsymbol{y} = \begin{bmatrix} Y_{1,1,1} \\ Y_{2,1,1} \\ \vdots \\ Y_{m,n,1} \\ \vdots \\ Y_{1,1,p} \\ Y_{2,1,p} \\ \vdots \\ Y_{m,n,p} \end{bmatrix}, \quad \boldsymbol{x} = \begin{bmatrix} \boldsymbol{b} \\ \boldsymbol{c} \end{bmatrix} = \begin{bmatrix} \beta_{1,1} \\ \beta_{1,2} \\ \vdots \\ \beta_{m,n} \\ c_{1,1} \\ c_{1,2} \\ \vdots \\ c_{m,n} \end{bmatrix}. \tag{2.4}$$

The variables $\boldsymbol{b}$ and $\boldsymbol{c}$ represent the values of β and at each point of the image, respectively. Then, the following model is considered

$$\boldsymbol{y} = A\boldsymbol{x} + \boldsymbol{\eta}, \tag{2.5}$$

where the matrix $A \in \mathbb{R}^{mnp \times 2mn}$ is

$$A = \begin{bmatrix} 4\Delta z f_1 & 0 & \dots & 0 & 1 & 0 & \dots & 0 \\ 0 & 4\Delta z f_1 & \dots & 0 & 0 & 1 & \dots & \vdots \\ \vdots & \vdots & \ddots & \vdots & \vdots & \vdots & \ddots & 0 \\ 0 & 0 & \dots & 4\Delta z f_1 & 0 & 0 & \dots & 1 \\ \vdots & \vdots & \vdots & \vdots & \vdots & \vdots & \vdots & \vdots \\ 4\Delta z f_p & 0 & \dots & 0 & 1 & 0 & \dots & 0 \\ 0 & 4\Delta z f_p & \dots & 0 & 0 & 1 & \dots & \vdots \\ \vdots & \vdots & \ddots & \vdots & \vdots & \vdots & \ddots & 0 \\ 0 & 0 & \dots & 4\Delta z f_p & 0 & 0 & \dots & 1 \end{bmatrix}, \tag{2.6}$$

and $\boldsymbol{\eta}$ represents white Gaussian noise. This assumption holds provided that the impulse responses of tissue reflectors at varying locations are uncorrelated, resulting in a probability density function that approximates a zero-mean Gaussian distribution [35].

Using least squares to recover $\boldsymbol{x}$ may result in solutions with high standard deviation due to the noise component. To mitigate this effect, regularization is introduced as $\mathcal{R}(\boldsymbol{x})$, turning the ACS estimation into the minimization of the cost function

$$\hat{\boldsymbol{x}} = \arg\min_{\boldsymbol{x}} \frac{1}{2} ||A\boldsymbol{x} - \boldsymbol{y}||_2^2 + \mathcal{R}(\boldsymbol{x}), \tag{2.7}$$

where μ is the regularization parameter. In existing literature [20], the isotropic total variation (TV) was selected as the regularization term,

$$\begin{aligned} \mathcal{R}(\boldsymbol{x}) &= \mu(\mathrm{TV}(\boldsymbol{b}) + \mathrm{TV}(\boldsymbol{c})), \\ \mathrm{TV}(\boldsymbol{v}) &= \sum_{i=1}^{mn} \sqrt{(\mathbf{D}_x v)_i^2 + (\mathbf{D}_y v)_i^2}, \end{aligned} \tag{2.8}$$

where μ is the regularization parameter, v is a vector representing an arbitrary flattened image of size $m \times n$, and $\mathbf{D}_x$ and $\mathbf{D}_y$ are the horizontal and vertical discrete derivative operators in matrix form, respectively. The solution that minimizes (2.7) with two terms of TV is calculated using the Alternating Direction Method of Multipliers [20].

2.3 Spatially Weighted Total Variation (SWTV-ACE)

Alternatively, the anisotropic version of the total variation has been tested with a spatially weighted version on the BSC term [30],

$$\begin{aligned} \mathcal{R}(\boldsymbol{x}) &= \mu_b \mathrm{TV}_{an}(\boldsymbol{b}) + \mu_c \mathrm{SWTV}_{an}(\boldsymbol{c}), \\ \mathrm{SWTV}_{an}(\boldsymbol{v}) &= \sum_{i=1}^{mn} |(W_{\mathrm{eSNR}} D_x v)_i| + |(W_{\mathrm{eSNR}} D_y v)_i|. \end{aligned} \tag{2.9}$$

The regularization parameters are μ_b and μ_c. The weight matrix $W_{\mathrm{eSNR}} \in \mathbb{R}^{mn \times mn}$ is a diagonal matrix that contains weights for each window, which are stacked on a vector w_{eSNR}, i.e., $W_{\mathrm{eSNR}} = \mathrm{Diag}(w_{\mathrm{eSNR}})$. These weights are computed from the difference between the envelope signal-to-noise ratio (eSNR) of the backscattered echoes and the expected eSNR of a Rayleigh distribution ($\mathrm{eSNR}_{ideal} \approx 1.913$). The eSNR deviation is calculated with

$$\Delta\mathrm{eSNR} = \frac{\mathrm{eSNR} - \mathrm{eSNR}_{ideal}}{\mathrm{eSNR}_{ideal}} \times 100\%, \tag{2.10}$$

and the weights are defined as

$$w_{\mathrm{eSNR}} = \frac{a_w}{1 + \exp[b_w(\Delta\mathrm{eSNR} - \Delta\mathrm{eSNR}_{\mathrm{min}})]}, \tag{2.11}$$

where a_w and b_w are hyperparameters that control the shape of the curve and $\Delta\mathrm{eSNR}_{\mathrm{min}}$ is a cut-off value. These are fixed to $a_w = 5$, $b_w = 0.09$, and $\Delta\mathrm{eSNR}_{\mathrm{min}} = 15$, as originally proposed in [30]. These values were selected based on their performance on a heterogeneous phantom. In this paper, the optimization problem with the new regularization weights is also solved with ADMM.

2.4 Proposed approach

This thesis presents a new inverse formulation for SLD that can be applied to media that exhibit changes in both backscatter and attenuation, termed Spatially-Weighted Image Fidelity and regularization Terms (SWIFT). In addition, it includes L1-norm regularization for changes in BSC instead of total variation, which further enhances the performance of the algorithm

2.4.1 L1-norm for BSC log difference

A new regularization function is proposed, which considers total variation for the attenuation term and L1-norm regularization for the backscatter term, i.e.,

$$\mathcal{R}(\boldsymbol{x}) = \mu_b \mathrm{TV}(\boldsymbol{b}) + \mu_c ||\boldsymbol{c}||_1. \tag{2.12}$$

This new prior is designed to yield results consistent with a piecewise homogeneous medium, where variations occur mainly at the boundaries between tissues. In this scenario, the term c, which represents the changes in backscatter, vanishes everywhere except at these boundaries. This is illustrated in Fig. 2.1, which shows the distribution of c from

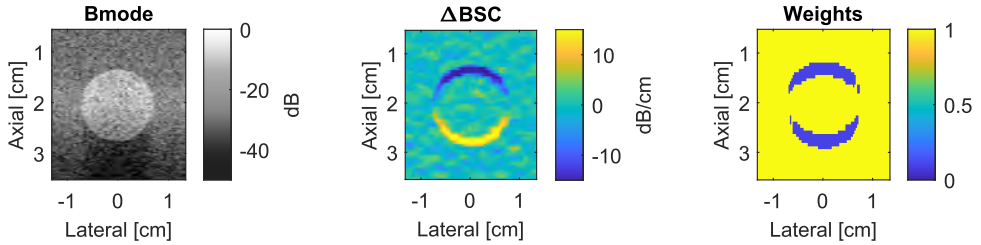

Figure 2.1: B-mode image, $\boldsymbol{c}_0$ map (ΔBSC), and spatial weights for a simulated phantom with an inclusion. The ΔBSC was obtained by solving the regularized inverse problem with no weights.

a hyperechoic simulated phantom. In this simulation, scattering was generated from a Gaussian distribution of density and different standard deviations for each region. The resulting image is sparse, which confirms that utilizing the L1 norm would be a more effective option for regularization than employing total variation. This decision aligns more closely with the underlying assumptions of the SLD model and facilitates a more effective reconstruction of the generated image.

2.4.2 Weighted fidelity and regularization

Spatially-varying weights can be computed from a first estimation of $\boldsymbol{x}$, denoted $\boldsymbol{x}_0 = [\boldsymbol{b}_0^T \quad \boldsymbol{c}_0^T]^T$, which is obtained by setting the weights to 1. Specifically, the term $\boldsymbol{c}_0$ is used because it indicates the location of tissue interfaces where the assumption of a uniform speckle pattern breaks down. Therefore, the weights are defined as

$$w = \begin{cases} 1, & \text{if } |c_0| < c_{th}, \\ w_0, & \text{otherwise.} \end{cases} \tag{2.13}$$

The constant w_0 represents the weights at tissue interfaces (close to 0), and c_{th} is the cut-off value for changes in BSC (measured in dB/cm). This relationship assigns a weight of 1 to homogeneous regions and a weight of w_0 to tissue boundaries. For the rest of the article, these hyperparameters are set to $w_0 = 0.1$ and $c_{th} = 10$ dB/cm. These hyperparameters were selected based on the performance in simulated media, measured by the root mean square error. An example of the weight map from a simulated phantom is displayed in Fig. 2.1.

The regularization weights can be extended to cover both attenuation and backscatter terms, rather than exclusively applying them to the backscatter term. This choice was made because a change of medium can come with changes in attenuation, so these regions should also be less regularized. Following (2.12), the new weighted regularization would be

$$\begin{aligned} \mathcal{R}(\boldsymbol{x}) &= \mu_b \text{SWTV}(\boldsymbol{b}) + \mu_c ||W\boldsymbol{c}||_1, \\ \text{SWTV}(\boldsymbol{u}) &= \sum_i \sqrt{(WD_x\boldsymbol{u})_i^2 + (WD_y\boldsymbol{u})_i^2}, \end{aligned} \tag{2.14}$$

where the matrix W is computed with $W = \text{Diag}(w)$, where w is calculated from (2.13).

Furthermore, to reduce artifacts at tissue interfaces, a weighting scheme in the data fidelity term $\mathcal{F}(\boldsymbol{x})$ is proposed, in which the norm of the squared differences is replaced with

$$\mathcal{F}(\boldsymbol{x}) = (\boldsymbol{y} - A\boldsymbol{x})^T \mathbf{W}^T \mathbf{W}(\boldsymbol{y} - A\boldsymbol{x}), \tag{2.15}$$

where $\mathbf{W} \in \mathbb{R}^{mnp \times mnp}$ is a diagonal matrix that carries the weight for each equation. These weights are assumed to be the same for each frequency but vary in the axial and lateral dimensions. They are obtained by applying axial min pooling to w from (2.13), using a kernel of 3 grid points to ensure information from windows that contain tissue boundaries is weighted accordingly. The new weight map $\tilde{w}$ is then utilized to compute the matrix $\mathbf{W} = \mathbf{I_p} \otimes \mathrm{Diag}(\tilde{w})$, where $\mathbf{I_p}$ is the identity matrix of size $p \times p$ and $\otimes$ is the Kronecker product. By some manipulation, one can define $\tilde{\boldsymbol{y}} := \mathbf{W}\boldsymbol{y}$ and $\tilde{A} := \mathbf{W}A$ and describe the new optimization goal

$$\hat{\boldsymbol{x}} = \arg\min_{\boldsymbol{x}} \left\{ \frac{1}{2} ||\tilde{\boldsymbol{y}} - \tilde{A}\boldsymbol{x}||^2 + \mathcal{R}(\boldsymbol{x}) \right\}, \tag{2.16}$$

which can be solved using the same optimization method as the previous approaches.

2.4.3 Optimization algorithm

To optimize the cost function, the matrix multiplication $\tilde{A}\boldsymbol{x}$ needs to be written in terms of $\boldsymbol{b}$ and $\boldsymbol{c}$, so the new optimization goal would be

$$\min_{\boldsymbol{b},\boldsymbol{c}} \left\{ \frac{1}{2} ||\tilde{\boldsymbol{y}} - A_1\boldsymbol{b} - A_2\boldsymbol{c}||_2^2 + \mathcal{R}(\boldsymbol{x}) \right\}, \tag{2.17}$$

where $\tilde{A} = [A_1\ A_2]$. Then, the optimization goal can be rewritten in the following form so it can be solved with ADMM by using an auxiliary variable $\boldsymbol{d}$:

$$\begin{aligned} &\min_{\boldsymbol{b},\boldsymbol{c},\boldsymbol{d}} \left\{ \frac{1}{2} ||\boldsymbol{d}||_2^2 + \mu_b \mathrm{SWTV}(\boldsymbol{b}) + \mu_c ||W\boldsymbol{c}||_1 \right\} \\ &\text{subject to} \quad A_1\boldsymbol{b} + A_2\boldsymbol{c} + \boldsymbol{d} = \tilde{\boldsymbol{y}}. \end{aligned} \tag{2.18}$$

Each term can be computed using Algorithm 1, where k is the iteration number. The initial values $\hat{\boldsymbol{b}}^0$ and $\hat{\boldsymbol{c}}^0$ are obtained by solving (2.16) with no regularization, meaning

$$\begin{bmatrix} \hat{\boldsymbol{b}}^0 \\ \hat{\boldsymbol{c}}^0 \end{bmatrix} = (\tilde{A}^T\tilde{A})^{-1}\tilde{A}^T\boldsymbol{x}. \tag{2.19}$$

The algorithm stops when the difference in the attenuation map between consecutive iterations is smaller than a threshold, i.e., $||\boldsymbol{b}^{k+1} - \boldsymbol{b}^k||^2 < 10^{-3}$. The sub-problem for $\boldsymbol{b}$ is solved using the iterative re-weighted least squares algorithm [36]. As for the sub-problem for $\boldsymbol{c}$, it is solved using a generalized iterative algorithm for Tikhonov regularization [37].

Algorithm 1 ADMM, scaled dual form

$\rho \leftarrow 1$
$\boldsymbol{b}^0 \leftarrow \hat{\boldsymbol{b}}^0$
$\boldsymbol{c}^0 \leftarrow \hat{\boldsymbol{c}}^0$
$\boldsymbol{d}^0, \boldsymbol{v}^0 \leftarrow 0$
$k \leftarrow 0$
repeat
$\boldsymbol{b}^{k+1} \leftarrow \arg\min_{\mathbf{b}} \{\mu_b \mathrm{SWTV}(\mathbf{b}) + \frac{\rho}{2}||A_1\mathbf{b} + A_2\boldsymbol{c}^k + \boldsymbol{d}^k - \tilde{\boldsymbol{y}} + \boldsymbol{v}^k||_2^2\}$
$\boldsymbol{c}^{k+1} \leftarrow \arg\min_{\mathbf{c}} \{\mu_c||W\mathbf{c}||_1 + \frac{\rho}{2}||A_1\boldsymbol{b}^{k+1} + A_2\mathbf{c} + \boldsymbol{d}^k - \tilde{\boldsymbol{y}} + \boldsymbol{v}^k||_2^2\}$
$\boldsymbol{d}^{k+1} \leftarrow \arg\min_{\mathbf{d}} \{\frac{1}{2}||\mathbf{d}||_2^2 + \frac{\rho}{2}||A_1\boldsymbol{b}^{k+1} + A_2\boldsymbol{c}^{k+1} + \boldsymbol{d} - \tilde{\boldsymbol{y}} + \boldsymbol{v}^k||_2^2\}$
$\boldsymbol{v}^{k+1} \leftarrow A_1\boldsymbol{b}^{k+1} + A_2\boldsymbol{c}^{k+1} + \boldsymbol{d}^{k+1} - \tilde{\boldsymbol{y}} + \boldsymbol{v}^k$
$k \leftarrow k + 1$
until the stopping criterion is reached.

Chapter 3

Methods

3.1 Datasets

3.1.1 Simulations

Layered media and media with inclusions were simulated using the k-Wave toolbox [38] in MATLAB. A linear transducer with 0.3 mm pitch and a center frequency of 6.66 MHz was simulated. In transmission, fixed focusing was used, with a focal depth of 2 cm and a focal number of 2. Likewise, dynamic focusing was used on reception with a focal number of 2. In all simulations, scattering was generated from a Gaussian distribution of density, centered at 1000 kg/m^3, and different standard deviations for each region to achieve the desired echogenicity. The speed of sound was fixed at 1540 m/s. For diffraction compensation, 6 samples from a homogeneous reference phantom with ACS of 0.7 dB/cm/MHz were simulated.

Two-layered media were simulated with an interface located at 2 mm depth. Four distinct samples were created, denoted S1, S2, S3, and S4. For S1, only a change in attenuation was introduced; for S2, a 12 dB increase in backscatter was simulated when transitioning from the top to the bottom layer; and for S3, a 12 dB decrease was applied. The selected ACS values were 0.5 and 1 dB/cm/MHz for the top and bottom layers, respectively. Lastly, S4 shows a uniform attenuation map of 0.75 dB/cm/MHz and a 12 dB increase in backscatter. The B-mode images and the ideal ACS maps are shown in Figure 4.1.

Three samples of media with a 7mm-radius inclusion were simulated, denoted S5, S6, and S7. The selected attenuation was 0.5 dB/cm/MHz on the background and 1 dB/cm/MHz in the inclusion. As in layered media, the backscatter of the inclusion with respect to the background varied. Specifically, S5 featured equal backscatter, while S6 demonstrated a 12 dB increase in the inclusion, and S7 showed a 12 dB decrease. In addition, a sample with three different-sized inclusions (6, 5, and 4 mm) and varying echogenicities was also simulated. In this sample, denoted S8, the background ACS was 1 dB/cm/MHz, whereas two inclusions had an ideal ACS of 0.5 dB/cm/MHz. The B-mode images and the ideal ACS maps are shown in Figure 4.1 for S5-S7, and in Figure 4.3 for S8.

3.1.2 Multi-target phantom

Experiments were also performed using a physical phantom (CIRS, Norfolk, VA) with spherical inclusions. Three targets with varying backscatter compared to the background were selected for comparison. Acoustic properties of each region are given in Table 3.1. Diffraction effects of the transducer were compensated with data from another calibrated phantom, which had an ACS value of 0.53 dB/cm/MHz (CIRS, Norfolk, VA). Data was acquired with a SonixTouch (Analogic Ultrasound, Peabody, MA) scanner using a L14-5 linear transducer.

Target	**Speed of sound** [m/s]	**ACS** [dB/cm/MHz]	**ΔBSC** [dB]
BG	1542	0.55	0
P1	1538	0.97	-0.9
P2	1539	0.95	+10.1
P3	1539	0.95	-9.0

Table 3.1: Tissue properties for Background (BG) and targets (P1, P2 and P3) from the CIRS phantom. BSC was measured relative to the background at 3 MHz.

3.1.3 Clinical cases

The algorithm was tested using data from healthy livers and tumors from the thyroid and breast. In the liver, although only small changes in attenuation may occur, there are inhomogeneities due to the presence of vessels or other tissue structures. In the images of tumors, there are simultaneous changes in both backscatter and attenuation. The acquisitions were approved by the ethics committee of the participating institutions, and all volunteers were required to sign an informed consent.

Liver examinations from two healthy volunteers were performed using a Verasonics Vantage NXT scanner (Redmond, WA, USA) with a C5-2v curved probe. The regions for ACS imaging were located at least 2 cm below the liver capsule, to avoid possible reverberation artifacts [39].

Ultrasound scans of the thyroid were performed using the same scanner described for the phantom acquisitions. The scan was conducted as part of an ultrasound-guided fine needle aspiration biopsy. Three nodules showing posterior acoustic enhancement were selected for testing. These nodules were classified in the Bethesda II category and categorized as benign colloid nodules. Additionally, four acquisitions from a calibrated reference phantom were employed for diffraction compensation. This phantom contained embedded spherical glass beads of $18.2 \pm 1\mu$m diameter, randomly distributed in an agar-based matrix at a concentration of 78.12 spheres per mm^3. Attenuation within the frequency band of the reference phantom was determined by fitting a second-order polynomial to the attenuation measured by the planar reflection method for each frequency, as described in [40]. Rectangular imaging regions that encompassed both parenchymal thyroid tissue and a nodule were selected for attenuation imaging.

An ultrasound examination of a breast tumor was conducted with the same scanner referenced in the preceding subsection as part of a core needle biopsy procedure. The

biopsy results classified the tumor as a benign complex fibroepithelial lesion (adenosis and usual hyperplasia). Diffraction compensation was performed using the same reference phantom as in the thyroid acquisitions.

3.2 Implementation details

The performance of the proposed approach (SWIFT), is compared with the regularization by isotropic total variation (RSLD) and the spatially weighted regularization on the BSC (SWTV-ACE). Power spectra estimation was performed using data blocks of 8 wavelengths laterally and 12 wavelengths axially, with an overlap of 80%. In the case of the liver acquisition, estimation was performed in the polar domain, considering 8 scan lines and a window of 12 wavelengths axially. These window sizes were empirically set to the smallest values that allowed for accurate image reconstruction and remained fixed throughout the study. These sizes also closely align with the optimal axial and lateral resolutions for estimating the backscatter coefficient [41].

The usable frequency range for ACS estimation was determined by identifying the -20 dB cutoff points within the frequency spectrum of each imaging region. The overlapping band across all imaging regions in each dataset was selected. This was from 3.5 to 8.5 MHz for the simulated data, from 2.5 to 7.5 MHz for the physical phantom, from 1.5 to 4 MHz in the liver acquisitions, and from 3.5 to 8 MHz for the thyroid and breast acquisitions.

In simulated media and the phantom acquisitions, the regularization parameters of each method were selected on a case-by-case basis, such that the root mean square error compared to the ground truth ACS in the whole image was minimized. Fixed regularization parameters were chosen for the clinical data. These were equal to the optimal values in the heterogeneous phantoms, reduced by a third ($\approx 10^{-0.5}$) to avoid over-regularization. These were $\mu = 10^{2.5}$ for RSLD, $\mu_b = 10^{2.5}$ and $\mu_c = 10^{-0.5}$ for SWTV-ACE, and $\mu_b = 10^{3}$ and $\mu_c = 10^{0.5}$ for SWIFT.

3.3 Evaluation metrics

To assess the performance of each algorithm, the normalized bias (NBias), normalized root mean square error (NRMSE), and contrast-to-noise ratio (CNR) were calculated for each simulation sample and each phantom acquisition. The NBias and NRMSE are defined as

$$\text{NBias} = \frac{1}{\beta_{GT}} \frac{1}{N} \sum_{i=1}^{N} (\hat{\beta}_i - \beta_{GT}), \tag{3.1}$$

$$\text{NRMSE} = \frac{1}{\beta_{GT}} \sqrt{\frac{1}{N} \sum_{i=1}^{N} (\hat{\beta}_i - \beta_{GT})^2}, \tag{3.2}$$

where $\hat{\beta}_i$ corresponds to the estimated ACS at a certain point in the image, β_{GT} corresponds to the ground truth, and N is the total number of points. Lastly, the CNR is defined as:

$$\text{CNR} = \frac{|\bar{\beta}_1 - \bar{\beta}_2|}{\sqrt{\text{Var}(\beta_1) + \text{Var}(\beta_2)}} \tag{3.3}$$

where $\bar{\beta}_i$ and $\mathrm{Var}(\beta_i)$ denote the mean and variance of the estimated ACS within a region. These metrics were calculated considering a 1 mm distance from the interface of both regions.

For the clinical data, only the mean and standard deviation of ACS were computed for each region. In addition, to verify the accuracy of the proposed methods in thyroid and breast tumors, the acoustic enhancement at the maximum frequency in the usable frequency range was calculated. The highest frequency was selected as it provided the best spatial resolution. To do this, the radiofrequency data was filtered around $f_c = 8$ MHz using a 2nd-order Butterworth digital filter with time reversal for phase compensation. The cut-off frequencies of the filter were 0.5 MHz below and above the central frequency (-6dB). Afterwards, the enhancement was defined as the difference in dB between the average signal envelope in a region below the tumor and the average from an adjacent region at the same depth, but passing through unaffected tissue. This value can be related to the difference in ACS between the two regions, $\Delta\beta$, by

$$AE = 2D\Delta\beta f_c, \tag{3.4}$$

where D is the tumor thickness along the wave propagation path and AE is the predicted enhancement from the attenuation maps. Specifically, the difference between this value and the measured enhancement from the B-mode image AE_{Bm} was calculated.

$$\Delta AE = AE - AE_{Bm} \tag{3.5}$$

This process was repeated in the physical phantom acquisitions for validation at 7.5 MHz, the highest frequency in the usable frequency range for the phantom data.

Chapter 4

Testing and validation

4.1 Results

4.1.1 Simulations

Fig. 4.1 shows the estimated attenuation maps for each method in simulated layered media and media with inclusions. Axial and lateral variations in attenuation can be observed in Fig. 4.2. In layered media, all lines were averaged to produce the axial profile. In data with inclusions, five vertical lines centered at $x = 0$ cm were averaged for the axial profiles, and five horizontal lines centered at $z = 2$ cm were averaged for the lateral profiles. In addition, metrics for the simulated data are displayed in Table 4.1.

In layered media, the performance of RSLD is severely degraded in the presence of BSC discontinuities, which can be observed by comparing the ACS map obtained from S1 with the ones obtained from S2, S3, or S4. An artifact is observed at the interface, where an axial increase in backscatter causes an underestimation of ACS, and a decrease causes an overestimation of ACS. The incorporation of weights by the SWTV-ACE method demonstrates notable improvement, resulting in a reduction of the NRMSE by over 10%. However, the overall performance still does not match that of sample S1. In contrast, SWIFT achieves an improved attenuation estimation, with a lower NRMSE than SWTV-ACE in most cases. This is more evident in the axial profiles for simulations S2 and S3, displayed in Fig. 4.2, where the mean ACS follows the ground truth very closely outside the tissue interface. In addition, these cases exhibit more than a 4-fold increase in CNR compared to SWTV-ACE.

In the simulated phantoms with inclusions, when no backscatter changes occur (S5), similar performance is observed among the three methods, just as in layered media. However, in cases where the backscatter varies, the proposed approach generates a map that closely resembles the ideal ACS in terms of shape and accuracy. In addition, from Fig. 4.2, an increase in resolution can be observed axially, as well as a reduction of variability within each homogeneous region, which is reflected in the NRMSE. The lowest NRMSE and the highest CNR in the heterogeneous samples are achieved by SWIFT.

Results from a sample with multiple inclusions in the field of view are shown in Figure 4.3, and the evaluation metrics for each inclusion and the background are displayed in Table 4.2. The image generated by SWIFT has two clearly visible attenuation inclusions, resembling the ground truth. Although the NRMSE is higher than in the other simula-

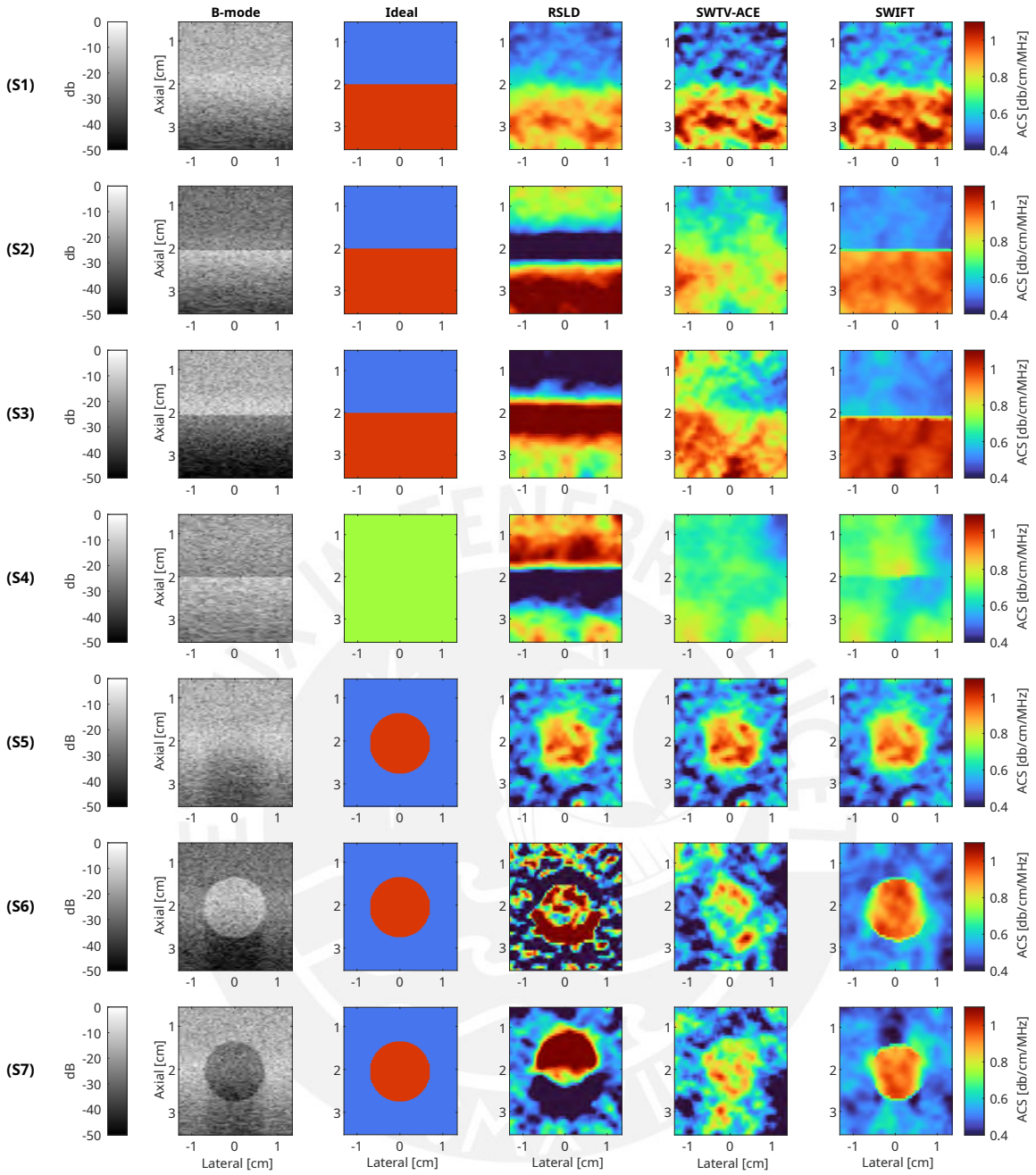

Figure 4.1: Ground-truth ACS and ACS reconstructions for each method in simulated data with layers (S1 to S4) and an inclusion (S5 to S7). The last column is the proposed approach.

tions, the resulting image still has a lower bias and NRMSE in all regions compared to the other two algorithms. This last metric is reduced by 43.6% on average when compared to RSLD and by 25.5% compared to SWTV-ACE.

In addition, the effect of each term of the proposed approach was explored. Three variations of the method were assessed with simulations S5 and S6, and the results are displayed in Figure 4.4. In the first (SWIFT-v1), the L1 norm was replaced with a Total Variation prior. This approach has a higher bias, especially in the inclusion. In

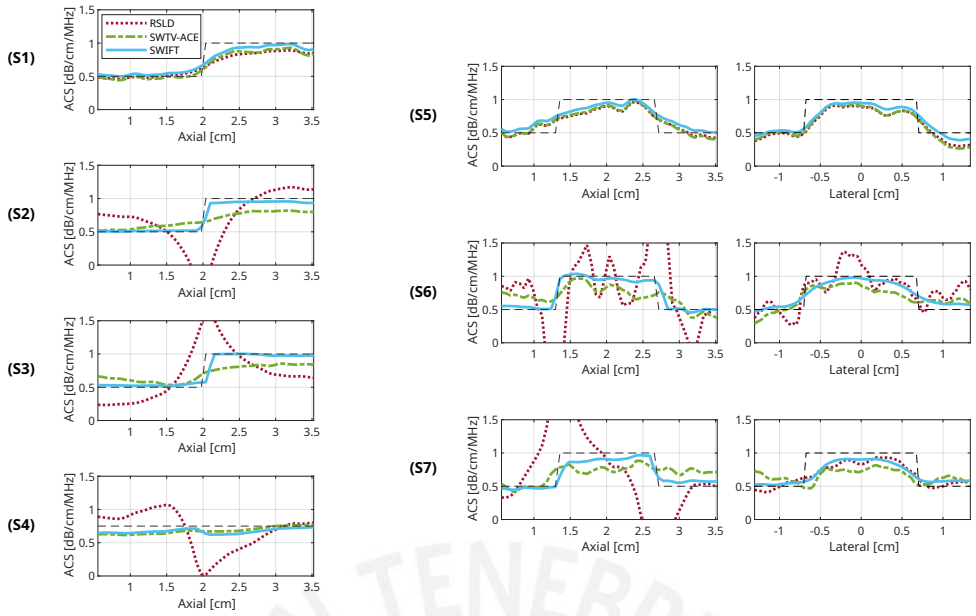

Figure 4.2: Axial and lateral variations in ACS. Each row represents a simulation. Ground truth is delineated with dashed black lines.

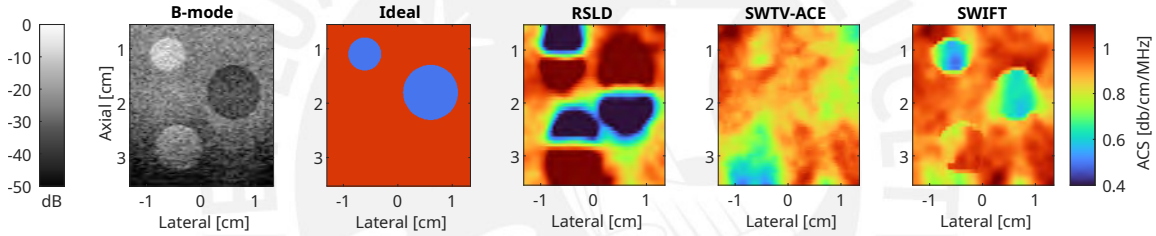

Figure 4.3: Attenuation maps from heterogeneous simulation with multiple inclusions (S8).

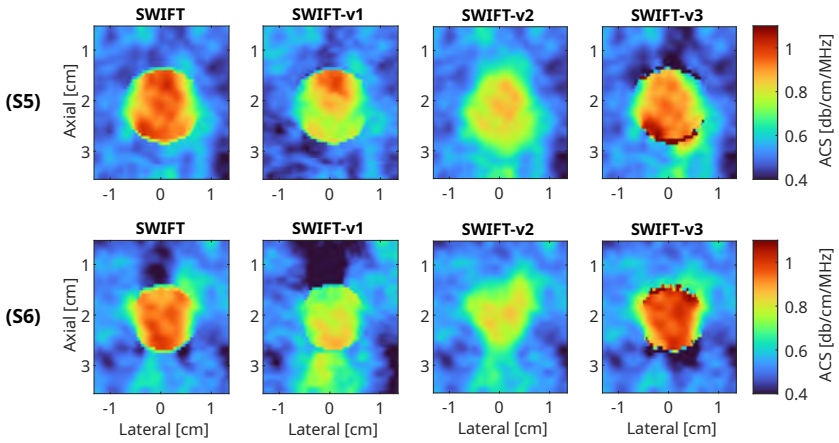

Figure 4.4: Attenuation maps from heterogeneous simulations with each variation of SWIFT. (v1) L1 norm replaced with TV. (v2) Regularization term without weights. (v3) Fidelity term without weights.

Sample	Method	NBias [%]		NRMSE [%]		CNR
		R1	R2	R1	R2	-
S1	RSLD	4.3	-14.1	**8.8**	15.6	**4.4**
	SWTV-ACE	**0.3**	-11.6	12.3	16.3	3.0
	SWIFT	10.3	**-6.0**	14.3	**11.4**	3.6
S2	RSLD	20.3	-6.6	47.6	32.5	0.9
	SWTV-ACE	25.7	-20.1	29.3	21.4	1.7
	SWIFT	**5.8**	**-5.9**	**7.1**	**6.8**	**10.6**
S3	RSLD	**-0.8**	-2.0	47.7	28.1	1.3
	SWTV-ACE	35.1	-9.7	40.2	12.4	1.8
	SWIFT	7.6	**0.4**	**9.7**	**4.0**	**9.4**
S4	RSLD	29.9	-19.8	44.8	29.5	-
	SWTV-ACE	-21.7	**-3.2**	24.4	**6.0**	-
	SWIFT	**-15.0**	-7.8	**21.6**	9.9	-
S5	RSLD	**5.7**	-11.8	15.9	13.8	3.4
	SWTV-ACE	5.0	-10.5	16.5	12.7	3.5
	SWIFT	6.5	**-12.1**	**14.3**	**13.6**	**3.9**
S6	RSLD	-3.5	**-6.1**	85.1	32.3	0.9
	SWTV-ACE	5.8	-25.9	26.6	27.8	1.3
	SWIFT	**2.9**	-8.3	**9.8**	**10.1**	**5.4**
S7	RSLD	**4.1**	**-8.6**	43.4	71.5	0.5
	SWTV-ACE	8.6	-20.3	27.6	21.6	1.7
	SWIFT	4.9	-10.2	**11.7**	**12.4**	**4.2**

Table 4.1: Evaluation metrics for each simulated sample. The first four samples (S1 to S4) correspond to layered media, in which region R1 corresponds to the top layer and region R2 to the bottom layer. The remaining samples (S5 to S8) represent media with inclusions, in which regions R1 and R2 represent the background and inclusion, respectively.

the second variation (SWIFT-v2), the spatially varying weights in the regularization term were removed. The resulting image has an over-smoothed attenuation map with no artifacts. Lastly, the third variation (SWIFT-v3) removes the weights in the fidelity term. In this image, there are artifacts at the top and bottom of the inclusion.

The number of iterations and execution times of each algorithm for the simulated data are displayed in Table 4.3. The algorithms were implemented in MATLAB 2024a and executed on a 12th-generation Intel Core i7 with a base clock speed of 2.1 GHz. The computation of the weight maps for SWTV-ACE and SWIFT (initial estimation) is not considered. SWTV-ACE requires the highest number of iterations and execution time, which indicates slower convergence.

Method	NBias [%]				NRMSE[%]			
	Bgnd.	I1	I2	I3	Bgnd.	I1	I2	I3
RSLD	-11.0	36.9	35.3	-12.4	32.6	77.0	99.8	39.4
SWTV-ACE	-12.8	65.5	66.3	-26.6	16.3	65.8	67.0	27.2
SWIFT	**-5.9**	**15.6**	**33.6**	**-9.1**	**8.7**	**18.5**	**35.8**	**11.3**

Table 4.2: Evaluation metrics for S8. Regions I1, I2, and I3 correspond to the top, middle, and bottom inclusions, respectively, and Bgnd. is the background.

Method	Iterations			Execution Time [s]		
	Min	Median	Max	Min	Median	Max
RSLD	6	7.5	27	0.68	1.46	2.18
SWTV-ACE	18	31.5	100	4.23	11.40	36.78
SWIFT	7	14.5	28	0.40	1.23	2.11

Table 4.3: Number of iterations and execution time of each algorithm for the simulated data. The image size was 49x89 in the lateral and axial dimensions, respectively, and the spectral ratios had 77 frequency points.

4.1.2 Multi-target phantom

Results for the calibrated phantom data are shown in Fig. 4.5. The isoechoic target has similar results for all methods, which is consistent with results from simulated data. In the targets with varying backscatter, artifacts are visible at the top and bottom of the inclusion when using RSLD with TV regularization. Introducing weights in the BSC term alleviates this issue at the cost of over-smoothing the attenuation map. Nonetheless, when using SWIFT, both the hyperechoic and hypoechoic targets have better-outlined shapes than in any other method.

Table 4.4 shows metrics for the three acquisitions. In the isoechoic target (P1), all approaches show similar performance. The ACS map from both the hyperechoic target (P2) and the hypoechoic target (P3) shows a significant reduction in NRMSE when using SWTV-ACE. However, there is poor contrast, which is reflected in the bias of both the background and inclusion. The lowest NRMSE in these cases was achieved by SWIFT, and the CNR was improved in all cases. Particularly, for the second and third targets, there is a 3.6-fold and a 2.6-fold increase in CNR compared to SWTV-ACE, respectively. As for the acoustic enhancement, the method that had the lowest difference between the B-mode image and the attenuation map was the one obtained by RSLD, followed by SWIFT.

4.1.3 Clinical data

Attenuation images were generated for each acquisition. Fig. 4.6 displays the attenuation maps produced from each imaging region in the liver. There are artifacts caused by heterogeneities in backscatter, pointed by white arrows, which are reduced by both SWTV-ACE and SWIFT. Table 4.5 compares the mean ACS of each liver sample, along with the standard deviation within the region of interest. Both methods reduce the stan-

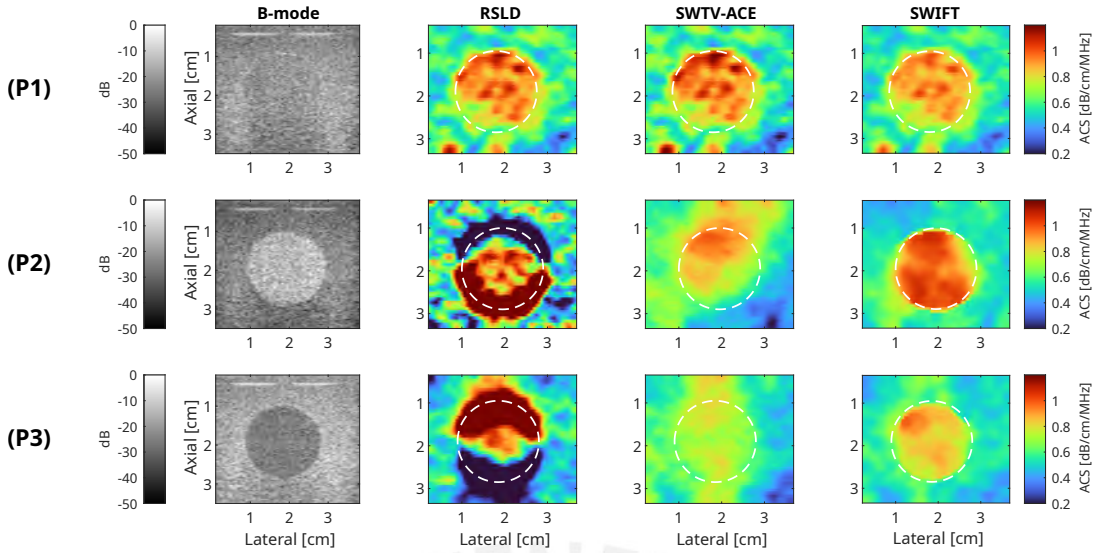

Figure 4.5: B-mode image from physical phantom data and reconstructions for each method. The left, middle, and right columns represent targets P1, P2, and P3, respectively.

Case	Method	NBias [%]		NRMSE [%]		CNR	ΔAE
		Bgnd.	Inc.	Bgnd.	Inc.		[dB]
P1	RSLD	6.3	-6.3	20.5	**11.7**	2.3	**1.9**
	SWTV-ACE	5.9	**-6.2**	21.9	12.2	2.1	2.3
	SWIFT	**2.2**	-9.8	**17.0**	12.6	**2.6**	2.2
P2	RSLD	-2.1	**1.7**	60.9	43.7	0.8	**0.9**
	SWTV-ACE	10.4	-15.5	27.7	19.5	1.1	7.3
	SWIFT	**0.4**	2.8	**12.5**	**8.2**	**4.2**	**0.9**
P3	RSLD	-4.2	**-9.2**	50.4	81.8	0.4	**0.0**
	SWTV-ACE	4.5	-24.3	20.3	24.7	1.2	5.3
	SWIFT	**-2.8**	-12.7	**11.5**	**14.1**	**3.5**	1.2

Table 4.4: Performance metrics for each regularization approach in a physical phantom. An isoechoic (P1), hyperechoic (P2) and hypoechoic (P3) targets were selected.

dard deviations in each scan compared to RSLD, by a factor of 2.2 for SWTV-ACE and 2.3 for SWIFT on average.

Attenuation maps generated from the thyroid and breast samples for each approach are depicted in Fig. 4.7. Maps from RSLD have artifacts resembling those discussed in the previous subsection, around the interfaces between the nodule and the thyroid parenchyma. These artifacts are diminished when using SWTV-ACE; however, sharper changes in attenuation are obtained with SWIFT. The last case includes two ACS maps, which were generated independently, one enclosing a heterogeneous region and the other enclosing a homogeneous region. In the heterogeneous region, SWTV-ACE estimates a lower attenuation in the parenchyma than the proposed approach. Nonetheless, when selecting a homogeneous region, attenuation in the thyroid parenchyma is more consistent

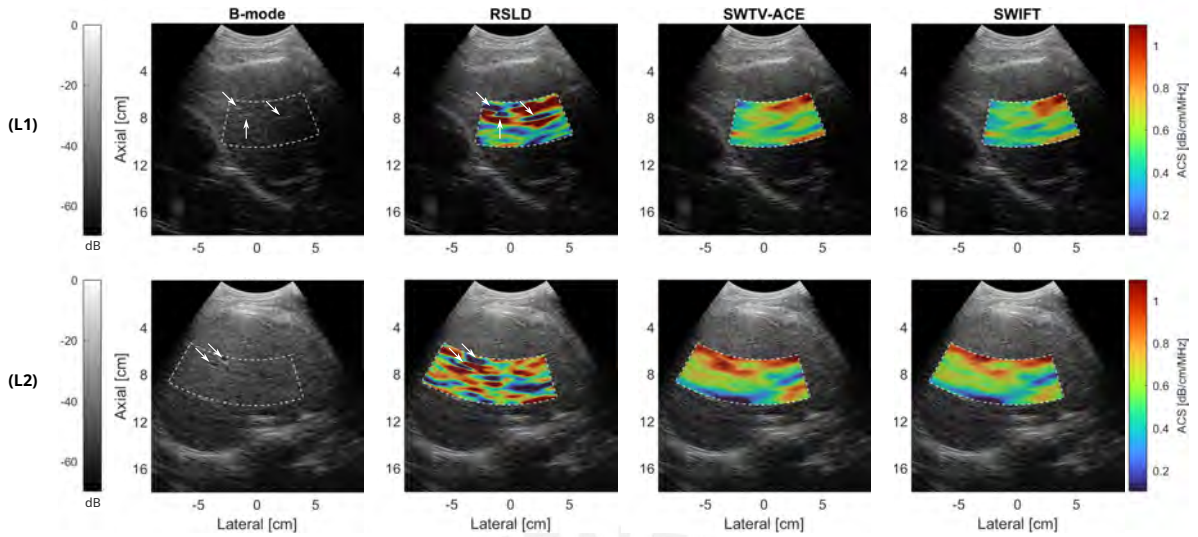

Figure 4.6: B-mode images and attenuation maps from liver acquisitions. The estimation regions were placed at least 2 cm below the liver capsule.

Case	ACS [dB/cm/MHz]		
	RSLD	**SWTV-ACE**	**SWIFT**
L1	0.61 ± 0.47	0.61 ± 0.17	0.58 ± 0.18
L2	0.64 ± 0.46	0.64 ± 0.25	0.61 ± 0.23

Table 4.5: Mean ACS and standard deviation of each liver acquisition.

with SWIFT.

The mean ACS values of each region are displayed along with their standard deviation in Table 4.6. The artifacts produced by RSLD are reflected in a higher standard deviation. The methods greatly differ in the attenuation measured on the thyroid nodules but are more consistent in the measurements from the thyroid parenchyma in the first two cases. The CNR and the difference between the AE from the attenuation maps and the B-mode image are also displayed. For the last case, the acoustic enhancement was calculated considering the mean attenuation of the homogeneous region. The proposed approach demonstrates a comparable CNR to SWTV-ACE and a higher CNR than RSLD. Notably, the predicted acoustic enhancement from the ACS maps aligns more closely with the measured acoustic enhancement from the B-mode images compared to SWTV-ACE.

Figure 4.7 shows attenuation maps of a benign breast mass. The image produced by RSLD is significantly affected by artifacts. Both SWTV-ACE and SWIFT produce images with reduced ACS measurements in the nodule; however, SWIFT offers better contrast. This is reflected in the CNR, shown in Table 4.6 along with the mean ACS in each region. The proposed approach also has better agreement of the measurements with the posterior acoustic enhancement.

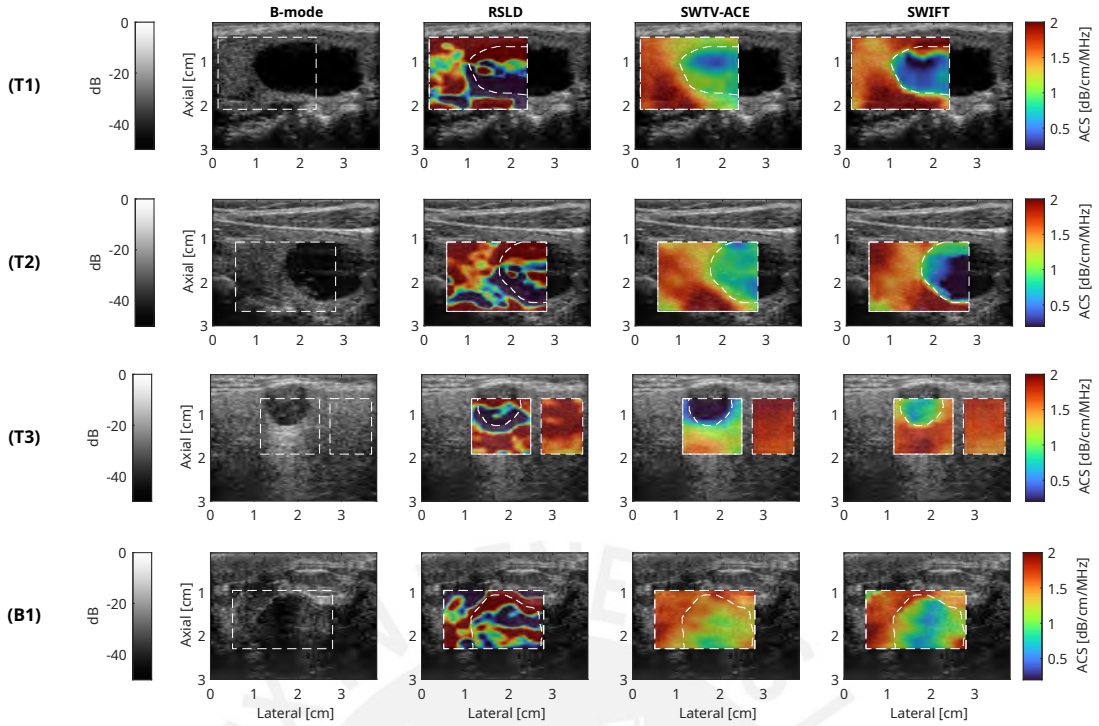

Figure 4.7: B-mode images and attenuation maps for benign thyroid nodules (T1-T3) and a breast lump (B1). Each row represents a different case. In T3, an ACS map was generated for a heterogeneous region (left) and a homogeneous region (right).

4.2 Discussion

In this work, a new regularization approach that increases estimation accuracy in heterogeneous media is proposed. Weights are applied in both the fidelity and regularization terms to deal with regions where the spectrum is not homogeneous. In addition, a change from Total Variation to an L1-norm on the backscatter term is proposed to account for model consistency.

Previous regularization approaches for SLD have limited performance in heterogeneous media. When only using Total Variation, as in RSLD, artifacts at tissue interfaces can arise because a change in BSC introduces a local offset in the frequency-attenuation curve, expressed in (2.2). This implies a trade-off between accuracy and the occurrence of artifacts: increasing regularization in BSC introduces artifacts, but decreasing it can lead to poor accuracy. Weighting the backscatter regularization term (SWTV-ACE) can reduce these artifacts; however, the approach is limited as it does not lead to an increase in estimation accuracy in media where attenuation varies too. As observed in Table 4.1, the NBias and NRMSE remain high, especially in layered media with varying BSC. In addition, the resulting attenuation maps in most cases remain with diffuse interfaces between media, as shown in Fig. 4.2, showcasing poor spatial resolution of the method. Another drawback of SWTV-ACE is that it assumes the envelope has a Rayleigh distribution, whereas other envelope statistical distributions could be more adequate [42], such as the general Nakagami distribution, used in [29]. The current approach does not make any assumptions about the envelope statistics of the echoes.

Case	Method	ACS [dB/cm/MHz]		CNR	ΔAE [dB]
		Tumor	Parenchyma		
T1	RSLD	0.43 ± 2.13	1.96 ± 1.71	0.56	3.1
	SWTV-ACE	0.8 ± 0.21	1.62 ± 0.29	2.24	-8.3
	SWIFT	0.52 ± 0.24	1.78 ± 0.32	**3.15**	**-1.1**
T2	RSLD	1.09 ± 2.12	1.72 ± 1.33	0.26	-11.6
	SWTV-ACE	0.86 ± 0.12	1.63 ± 0.28	2.52	-8.9
	SWIFT	0.36 ± 0.41	1.71 ± 0.33	**2.57**	**3.4**
T3–R1	RSLD	1.14 ± 1.39	1.55 ± 0.91	0.25	-2.7
	SWTV-ACE	-0.08 ± 0.3	1.12 ± 0.22	3.25	13.9
	SWIFT	0.86 ± 0.12	1.76 ± 0.18	**4.12**	**-1.1**
T3–R2	RSLD	-	1.84 ± 0.31	-	-
	SWTV-ACE	-	1.84 ± 0.14	-	-
	SWIFT	-	1.68 ± 0.12	-	-
B1	RSLD	1.02 ± 1.17	1.06 ± 1.72	0.02	-19.0
	SWTV-ACE	1.22 ± 0.18	1.64 ± 0.14	1.84	-7.5
	SWIFT	0.95 ± 0.23	1.62 ± 0.22	**2.07**	**0.1**

Table 4.6: ACS measurements and performance metrics of each method on the thyroid (T1-T3) and breast (B1) acquisitions. For T3, R1 represents the heterogeneous imaging region and R2 the homogeneous region.

Spatially varying weights in both fidelity and data terms tackle the artifacts effectively. Firstly, weights in the fidelity term penalize the equations that come from regions with changes in BSC. In these regions, not only might the estimation of spectra be flawed, but also the assumption of a constant, frequency-independent BSC ratio. The effect of the weights on both regularization terms is clear. By introducing little regularization in regions where there is likely an interface, this new approach favors rapid changes in attenuation during optimization, which can be observed in the lateral and axial profiles in Fig. 4.2. Furthermore, it also allows the algorithm to focus on smoothing homogeneous regions. This is also reflected in a reduction in NRMSE and an increase in CNR in both the simulated and phantom data.

The new approach was implemented using ADMM. In all simulated samples from this study, the algorithm consistently converged to the desired tolerance within a maximum of 28 iterations, showing low sensitivity to the choice of hyperparameters. This robust convergence rate suggests that SWIFT performs reliably across various parameter settings. In addition, although an analytical proof of solution uniqueness has not been derived, empirical evidence supports a high degree of consistency in the results. No substantially different solutions were obtained across trials, even when using different initializations, such as random values or zeroes. These findings indicate that the solution may be unique or, at the very least, does not exhibit significant divergence across different initializations within the tested conditions. Additionally, the estimation time remains lower than that of total variation, despite the increased number of iterations. This efficiency gain can be attributed to the incorporation of the L1-norm, which modifies one of the sub-steps in the ADMM framework (Algorithm 1). The resulting subproblem is solved using an efficient

implementation of generalized Tikhonov regularization [37]. Moreover, while this study does not explore further optimizations, this step could potentially be accelerated even further by employing faster algorithms such as ISTA or FISTA [43].

Attenuation measurements were conducted on the livers of three healthy volunteers. The average ACS remains within the range of normal attenuation values in non-steatotic livers, which is between 0.56 to 0.63 dB/cm/MHz (interquartile range in [44]). The methods have a percentual difference in mean value which is less than 5%, meaning they are consistent with each other. An important remark is that the liver parenchyma may have heterogeneous regions with different attenuation, so some variability in attenuation measurements within the region of interest is expected. However, the techniques reduce artifacts caused by small heterogeneities without over-smoothing the attenuation map.

The performance of the algorithms was also evaluated for the assessment of thyroid nodules and a breast lump. In both weighted approaches (SWTV-ACE and SWIFT), a clear distinction in the ACS between healthy thyroid tissue and nodules can be observed, although SWIFT allows sharper changes in the ACS maps. In addition, measurements of mean ACS in the thyroid parenchyma are consistent with the literature, with mean values ranging from 1.5 dB/cm/MHz [6] to 1.76 dB/cm/MHz [14]. In the case of colloid nodules, a lower attenuation is observed. It is important to note that previous reports did not include attenuation measurements for this type of nodule. Still, studies from other thyroid nodules report a low attenuation too [40][6]. In the case of the breast acquisition, the estimated ACS in the tumor was similar to measurements taken from other benign masses, such as fibroadenoma, which was from 0.51 to 1.29 dB/cm/MHz [7]. Attenuation in the breast parenchyma was also inside the usual range, considering the central frequency of the chosen bandwidth [45]. Furthermore, ACS measurements are consistent with the acoustic enhancement measured from the B-mode image, as observed in Table 4.6. In all cases, the predicted AE from the ACS maps is more consistent with what is observed in the B-mode image, compared to SWTV-ACE. The observed improvement in accuracy can be attributed to the weighting assigned to the fidelity term. This weighting grants less significance to areas with heterogeneities, yielding a more precise attenuation map. This may also explain the notable discrepancies observed between the attenuation maps generated by different algorithms.

The proposed technique has some limitations. Selecting the right hyperparameters to generate an accurate weight map is not trivial. Specifically, the cut-off value c_{th} in Eq. 2.13 varies when the window size is altered. Larger window sizes result in smoother changes in BSC, so the cut-off value should be lower. Unfortunately, this study does not delve into the comparative performance of different weight map configurations, leaving open questions about their impact on reconstruction accuracy. Future work could explore this aspect to further optimize the method.

Setting the regularization parameters can also be challenging. In this work, a fair comparison was sought by optimizing them with calibrated data (both simulated and experimental). The hyperparameters were fixed when analyzing the clinical data; however, better performance may be achieved with case-specific regularization weights. Their automatic selection based on the data was not addressed in this study, although several methods in the literature can tackle this issue, such as the L-curve method [46], the general information criterion [47], or even deep learning [48]. This presents a promising opportunity for future efforts. In addition, Figure 4.8 explores the effect of varying the

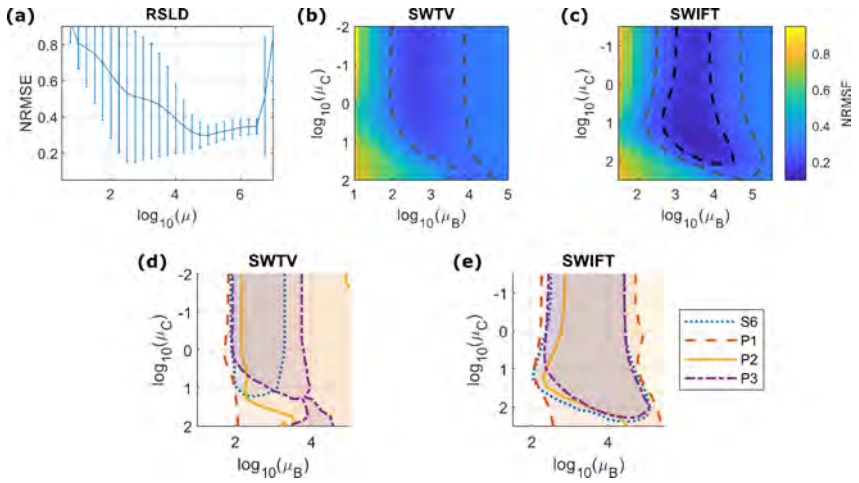

Figure 4.8: Effect of varying the regularization parameters on NRMSE with (a) RSLD, (b) SWTV-ACE, and (c) SWIFT. The NRMSE was averaged over four samples, with contour lines at 0.3 (gray) and 0.2 (black). Regions in which NRMSE<0.3 for each sample are shown in (d) and (e).

regularization parameters on the NRMSE. A simulated sample (S6) and all samples from the physical phantom with inclusions (P1, P2, and P3) were selected for comparison. Only the NRMSE in the inclusion was considered. Both RSLD and SWTV-ACE yield an average NRMSE higher than 20% for any choice of regularization parameter, while SWIFT can achieve a lower NRMSE. In addition, the regions where NRMSE<30% are shown for each simulation. In SWIFT, the overlapped areas are at least two orders of magnitude in length for μ_B and three orders of magnitude in length for μ_C. This suggests that SWIFT remains fairly resilient to variations in the regularization parameter, validating the use of fixed regularization weights for clinical data.

In addition, the current approach assumes the underlying medium to be piecewise homogeneous. In a more practical scenario, where this may not hold, the approach may not perform well. A more generalizable approach would be to include the second derivatives in the regularization term, allowing the resulting map to be piece-wise linear [49]. This has achieved better results in the field of ultrasound elastography [50, 51]. However, this would increase the number of hyperparameters involved.

Lastly, SWIFT utilizes a reference-based methodology, which may limit its advantage relative to modern reference-free techniques [28, 29]. Nevertheless, its core weighted inversion mechanism remains applicable within reference-free frameworks. Future work could consequently integrate both methodologies to enhance performance.

Conclusions

This study addresses the difficulties in attenuation imaging when changes in both backscatter and attenuation exist. The proposed approach, which incorporates spatially varying weights for both the fidelity and regularization terms and utilizes L1-norm regularization for changes in the backscatter coefficient, enhances the accuracy of ACS estimation in heterogeneous tissue. Simulated and experimental data acquired on calibrated phantoms verify the accuracy of the proposed approach and its superior performance when compared to other approaches used for benchmarking in this study. Preliminary *in vivo* validation with thyroid cases and a breast acquisition further demonstrates the robustness of the proposed method for reconstructing attenuation coefficient images from tissues in the presence of backscatter variations.

Bibliography

[1] Guy Cloutier, François Destrempes, François Yu, and An Tang, "Quantitative ultrasound imaging of soft biological tissues: a primer for radiologists and medical physicists," *Insights into Imaging*, vol. 12, pp. 1–20, Sep. 2021.

[2] Timothy A Bigelow and Yassin Labyed, "Attenuation compensation and estimation," *Quantitative ultrasound in soft tissues*, pp. 71–93, 2013.

[3] Thomas L Szabo, *Diagnostic ultrasound imaging: inside out*, Academic press, 2004.

[4] Giovanna Ferraioli and Livia Beatriz Soares Monteiro, "Ultrasound-based techniques for the diagnosis of liver steatosis," *World Journal of Gastroenterology*, vol. 25, no. 40, pp. 6053, 2019.

[5] Giovanna Ferraioli, Laura Maiocchi, Giovanni Savietto, Carmine Tinelli, Mara Nichetti, Mariangela Rondanelli, Fabrizio Calliada, Lorenzo Preda, and Carlo Filice, "Performance of the attenuation imaging technology in the detection of liver steatosis," *J. Ultrasound Med.*, vol. 40, no. 7, pp. 1325–1332, 2021.

[6] Yasutomo Fujii, Nobuyuki Taniguchi, Kouichi Itoh, and Kiyoka Omoto, "Attenuation coefficient measurement in the thyroid," *J. Ultrasound Med.*, vol. 22, no. 10, pp. 1067–1073, 2003.

[7] Kibo Nam, James A Zagzebski, and Timothy J Hall, "Quantitative assessment of in vivo breast masses using ultrasound attenuation and backscatter," *Ultrasonic Imaging*, vol. 35, no. 2, pp. 146–161, 2013.

[8] Barbara L McFarlin, Viksit Kumar, Timothy A Bigelow, Douglas G Simpson, Rosemary C White-Traut, Jacques S Abramowicz, and William D O'Brien Jr, "Beyond cervical length: A pilot study of ultrasonic attenuation for early detection of preterm birth risk," *Ultrasound Med. Biol.*, vol. 41, no. 11, pp. 3023–3029, 2015.

[9] Farah Deeba, Manyou Ma, Mehran Pesteie, Jefferson Terry, Denise Pugash, Jennifer A Hutcheon, Chantal Mayer, Septimiu Salcudean, and Robert Rohling, "Attenuation coefficient estimation of normal placentas," *Ultrasound Med. Biol.*, vol. 45, no. 5, pp. 1081–1093, 2019.

[10] Tadashi Yamaguchi, "Basic concept and clinical applications of quantitative ultrasound (qus) technologies," *J. Med. Ultrason.*, vol. 48, no. 4, pp. 391–402, 2021.

[11] Roberto Lavarello and Michael Oelze, "Quantitative ultrasound estimates from populations of scatterers with continuous size distributions: Effects of the size estimator algorithm," *IEEE transactions on ultrasonics, ferroelectrics, and frequency control*, vol. 59, no. 9, pp. 2066–2076, 2012.

[12] Michael L Oelze and Jonathan Mamou, "Review of quantitative ultrasound: Envelope statistics and backscatter coefficient imaging and contributions to diagnostic ultrasound," *IEEE transactions on ultrasonics, ferroelectrics, and frequency control*, vol. 63, no. 2, pp. 336–351, 2016.

[13] Aiguo Han, Michael P Andre, Lisa Deiranieh, Elise Housman, John W Erdman Jr, Rohit Loomba, Claude B Sirlin, and William D O'Brien Jr, "Repeatability and reproducibility of the ultrasonic attenuation coefficient and backscatter coefficient measured in the right lobe of the liver in adults with known or suspected nonalcoholic fatty liver disease," *Journal of Ultrasound in Medicine*, vol. 37, no. 8, pp. 1913–1927, 2018.

[14] Julien Rouyer, Tony Cueva, Tamy Yamamoto, Alberto Portal, and Roberto J Lavarello, "In vivo estimation of attenuation and backscatter coefficients from human thyroids," *IEEE Trans. Ultrason., Ferroelectr., Freq. Control*, vol. 63, no. 9, pp. 1253–1261, Feb. 2016.

[15] Kayvan Samimi and Tomy Varghese, "Performance evaluation of the spectral centroid downshift method for attenuation estimation," *IEEE Trans. Ultrason., Ferroelectr., Freq. Control*, vol. 62, no. 5, pp. 871–880, May 2015.

[16] Graham Treece, Richard Prager, and Andrew Gee, "Ultrasound attenuation measurement in the presence of scatterer variation for reduction of shadowing and enhancement," *IEEE Trans. Ultrason., Ferroelectr., Freq. Control*, vol. 52, no. 12, pp. 2346–2360, Dec. 2005.

[17] Kevin J Parker and Robert C Waag, "Measurement of ultrasonic attenuation within regions selected from b-scan images," *IEEE Trans. Biomed. Eng.*, , no. 8, pp. 431–437, Aug. 1983.

[18] Lin Xin Yao, James A Zagzebski, and Ernest L Madsen, "Backscatter coefficient measurements using a reference phantom to extract depth-dependent instrumentation factors," *Ultrasonic imaging*, vol. 12, no. 1, pp. 58–70, 1990.

[19] Yassin Labyed and Timothy A Bigelow, "A theoretical comparison of attenuation measurement techniques from backscattered ultrasound echoes," *J. Acoust. Soc. Amer.*, vol. 129, no. 4, pp. 2316–2324, 2011.

[20] Andres L Coila and Roberto Lavarello, "Regularized spectral log difference technique for ultrasonic attenuation imaging," *IEEE Trans. Ultrason., Ferroelectr., Freq. Control*, vol. 65, no. 3, pp. 378–389, Mar. 2018.

[21] Hyungsuk Kim and Tomy Varghese, "Hybrid spectral domain method for attenuation slope estimation," *Ultrasound Med. Biol.*, vol. 34, no. 11, pp. 1808–1819, 2008.

[22] Leander Claes, Sarah Johannesmann, Elmar Baumhögger, and Bernd Henning, "Quantification of frequency-dependent absorption phenomena," in *Proceedings of Meetings on Acoustics*. AIP Publishing, 2019, vol. 38.

[23] Dinah Maria Brandner, Xiran Cai, Josquin Foiret, Katherine W Ferrara, and Bernhard G Zagar, "Estimation of tissue attenuation from ultrasonic b-mode images—spectral-log-difference and method-of-moments algorithms compared," *Sensors*, vol. 21, no. 7, pp. 2548, 2021.

[24] Zara Vajihi, Ivan M Rosado-Mendez, Timothy J Hall, and Hassan Rivaz, "Low variance estimation of backscatter quantitative ultrasound parameters using dynamic programming," *IEEE Trans. Ultrason., Ferroelectr., Freq. Control*, vol. 65, no. 11, pp. 2042–2053, Nov. 2018.

[25] Hector Chahuara, Adrian Basarab, and Roberto Lavarello, "Regularized framework for simultaneous estimation of ultrasonic attenuation and backscatter coefficients," in *Proc. IEEE Int. Ultrason. Symp. (IUS)*, Sep. 2020, pp. 1–4.

[26] Noushin Jafarpisheh, Timothy J Hall, Hassan Rivaz, and Ivan M Rosado-Mendez, "Analytic global regularized backscatter quantitative ultrasound," *IEEE Trans. Ultrason., Ferroelectr., Freq. Control*, vol. 68, no. 5, pp. 1605–1617, Dec. 2020.

[27] José Timaná, Hector Chahuara, Lokesh Basavarajappa, Adrian Basarab, Kenneth Hoyt, and Roberto Lavarello, "Reducing the degrees of freedom for simultaneous estimation of ultrasonic attenuation and backscatter coefficients: Application to liver steatosis detection," in *Proc. IEEE Int. Ultrason. Symp. (IUS)*, Nov. 2023, pp. 1–4.

[28] Ping Gong, Pengfei Song, Chengwu Huang, Joshua Trzasko, and Shigao Chen, "System-independent ultrasound attenuation coefficient estimation using spectra normalization," *IEEE Trans. Ultrason., Ferroelectr., Freq. Control*, vol. 66, no. 5, pp. 867–875, May 2019.

[29] Iman Rafati, François Destrempes, Ladan Yazdani, Marc Gesnik, An Tang, and Guy Cloutier, "Regularized ultrasound phantom-free local attenuation coefficient slope (ACS) imaging in homogeneous and heterogeneous tissues," *IEEE Trans. Ultrason., Ferroelectr., Freq. Control*, vol. 69, no. 12, pp. 3338–3352, Nov. 2022.

[30] Farah Deeba, Caitlin Schneider, Shahed Mohammed, Mohammad Honarvar, Edward Tam, Septimiu Salcudean, and Robert Rohling, "SWTV-ACE: Spatially weighted regularization based attenuation coefficient estimation method for hepatic steatosis detection," in *Medical Image Computing and Computer Assisted Intervention – MICCAI 2019*, Cham, 2019, pp. 610–618, Springer International Publishing.

[31] Jasleen Birdi, Jan D'hooge, and Alexander Bertrand, "Spatially variant ultrasound attenuation mapping using a regularized linear least-squares approach," *IEEE Trans. Ultrason., Ferroelectr., Freq. Control*, vol. 69, no. 5, pp. 1596–1609, Mar. 2022.

[32] Noushin Jafarpisheh, Laura Castaneda-Martinez, Hayley Whitson, Ivan M Rosado-Mendez, and Hassan Rivaz, "Physics-inspired regularized pulse-echo quantitative

ultrasound: Efficient optimization with ADMM," *IEEE Trans. Ultrason., Ferroelectr., Freq. Control*, Oct. 2023.

[33] Sebastian Merino and Roberto Lavarello, "Spatially-weighted inverse formulation for enhanced ultrasound attenuation imaging," in *2024 IEEE International Symposium on Biomedical Imaging (ISBI)*, 2024, pp. 1–4.

[34] Sebastian Merino and Roberto Lavarello, "Spatially weighted fidelity and regularization terms for attenuation imaging," *IEEE Transactions on Ultrasonics, Ferroelectrics, and Frequency Control*, vol. 72, no. 3, pp. 338–350, 2025.

[35] Roman Kuc and Mischa Schwartz, "Estimating the acoustic attenuation coefficient slope for liver from reflected ultrasound signals," *IEEE Transactions on Sonics and Ultrasonics*, vol. 26, no. 5, pp. 353–361, 1979.

[36] Paul Rodríguez, "Total variation regularization algorithms for images corrupted with different noise models: a review," *Journal of Electrical and Computer Engineering*, vol. 2013, pp. 10–10, 2013.

[37] R. Lavarello, F. Kamalabadi, and W.D. O'Brien, "A regularized inverse approach to ultrasonic pulse-echo imaging," *IEEE Transactions on Medical Imaging*, vol. 25, no. 6, pp. 712–722, 2006.

[38] Bradley E Treeby, Jiri Jaros, Alistair P Rendell, and BT Cox, "Modeling nonlinear ultrasound propagation in heterogeneous media with power law absorption using k-space pseudospectral method," *J. Acoust. Soc. Amer.*, vol. 131, no. 6, pp. 4324–4336, 2012.

[39] Katsutoshi Sugimoto, Masakazu Abe, Hisashi Oshiro, Hiroshi Takahashi, Tatsuya Kakegawa, Yusuke Tomita, Yu Yoshimasu, Hirohito Takeuchi, and Takao Itoi, "The most appropriate region-of-interest position for attenuation coefficient measurement in the evaluation of liver steatosis," *J. Med. Ultrason.*, vol. 48, no. 4, pp. 615–621, Aug. 2021.

[40] Andres Coila, Rosa Laimes, Claudia Salazar, Julien Rouyer, Gabriel Jimenez, Joseph A Pinto, Jorge Guerrero, and Roberto Lavarello, "In vivo attenuation estimation in human thyroid nodules using the regularized spectral log difference technique: Initial pilot study," in *Proc. IEEE Int. Ultrason. Symp. (IUS)*, Sep. 2017, pp. 1–4.

[41] Michael L Oelze and William D O'Brien Jr, "Defining optimal axial and lateral resolution for estimating scatterer properties from volumes using ultrasound backscatter," *The Journal of the Acoustical Society of America*, vol. 115, no. 6, pp. 3226–3234, 2004.

[42] François Destrempes and Guy Cloutier, "Review of envelope statistics models for quantitative ultrasound imaging and tissue characterization," in *Quantitative ultrasound in soft tissues*, pp. 107–152. Springer, 2023.

[43] Amir Beck and Marc Teboulle, "A fast iterative shrinkage-thresholding algorithm for linear inverse problems," *SIAM journal on imaging sciences*, vol. 2, no. 1, pp. 183–202, 2009.

[44] Toshifumi Tada, Hiroko Iijima, Natsuko Kobayashi, Masahiro Yoshida, Takashi Nishimura, Takashi Kumada, Reiichiro Kondo, Hirohisa Yano, Masayoshi Kage, Chikage Nakano, et al., "Usefulness of attenuation imaging with an ultrasound scanner for the evaluation of hepatic steatosis," *Ultrasound Med. Biol.*, vol. 45, no. 10, pp. 2679–2687, Oct. 2019.

[45] FT d'Astous and FS Foster, "Frequency dependence of ultrasound attenuation and backscatter in breast tissue," *Ultrasound in medicine & biology*, vol. 12, no. 10, pp. 795–808, 1986.

[46] Per Christian Hansen, "The L-curve and its use in the numerical treatment of inverse problems," 1999.

[47] Yiyun Zhang, Runze Li, and Chih-Ling Tsai, "Regularization parameter selections via generalized information criterion," *Journal of the American statistical Association*, vol. 105, no. 489, pp. 312–323, 2010.

[48] Babak Maboudi Afkham, Julianne Chung, and Matthias Chung, "Learning regularization parameters of inverse problems via deep neural networks," *Inverse Problems*, vol. 37, no. 10, pp. 105017, 2021.

[49] Joaquim Campos, Shayan Aziznejad, and Michael Unser, "Learning of continuous and piecewise-linear functions with hessian total-variation regularization," *IEEE Open Journal of Signal Processing*, vol. 3, pp. 36–48, 2021.

[50] Md Ashikuzzaman and Hassan Rivaz, "Second-order ultrasound elastography with l1-norm spatial regularization," *IEEE Transactions on Ultrasonics, Ferroelectrics, and Frequency Control*, vol. 69, no. 3, pp. 1008–1019, 2022.

[51] Md Ashikuzzaman, Bo Peng, Jingfeng Jiang, and Hassan Rivaz, "Alternating direction method of multipliers for displacement estimation in ultrasound strain elastography," *Medical physics*, vol. 51, no. 5, pp. 3521–3540, 2024.